Time-resolved measurements of desorbed gas during 1-MeV K^+ pulsed beam deposition in a stainless steel target

F. M. Bieniosek,* L. R. Prost,† and P. A. Seidl

Lawrence Berkeley National Laboratory, Heavy Ion Fusion Science Virtual National Laboratory, 1 Cyclotron Road, Berkeley, California 94720, USA

A. W. Molvik and M. Kireeff Covo

Lawrence Livermore National Laboratory, Heavy Ion Fusion Science Virtual National Laboratory, Livermore, California 94550, USA

(Received 3 April 2007; published 5 September 2007)

Measurements were made of the density, species, and velocity of the desorbed gas cloud on intense K^+ beam bombardment of a stainless steel target. Residual gas analyzer measurements indicate that the gas cloud consists of predominantly H_2. Energy analyzer measurements of doubly ionized beam ions show that the ratio of hydrogen gas production to beam density was approximately 3000 molecules/ion at normal incidence. Optical measurements of the evolution of the gas cloud during the beam pulse show a distribution with an average expansion velocity of about 0.5 mm/μs. Comparison is made with a simple model of the gas cloud behavior.

DOI: 10.1103/PhysRevSTAB.10.093201 PACS numbers: 52.59.−f, 52.70.Kz, 52.58.Hm

I. INTRODUCTION

Beams of heavy ions release large amounts of neutral gas when they strike the vacuum wall. This effect [1], and the related problem of the electron cloud [2], can have a serious deleterious effect by causing a local pressure rise that limits the performance of particle accelerators. Based on measurements of pressure rise, the desorption coefficients have previously been determined to be about 10 000 for 1 MeV K^+ ions at near grazing incidence on stainless steel walls [3].

A technique in wide use to determine the coefficient of gas desorption (the ratio of desorbed gas molecules to beam ions) is to measured the local pressure rise due to ion beams striking a target, aperture, or chamber wall, by the use of a calibrated pressure gauge. Knowledge of the volume of the test chamber and the pumping speed allows the calculation of the amount of desorbed gas from the beam induced pressure rise assuming equilibration of the desorbed gas in the vacuum chamber after many collisions with the wall [4].

We develop here two new independent techniques of estimating the gas production. The first technique is based on measurement of the flux of K^{++} ions produced by ionization of incident K^+ beam ions $K^+ \rightarrow K^{++}$ in the gas cloud. As the ion beam strikes a solid target, it desorbs gas trapped on or near the surface of the wall. The K^{++} ions are generated by ionization of the incident K^+ ion beam by the gas cloud created at the entrance slit of the analyzer or at the hole plate upstream of the analyzer. The intensity of the K^{++} ion signal provides an estimate of the rate of production of the gas cloud. Thereby the rate and number of gas molecules instantaneously released per incident beam ion on the wall under the conditions of this experiment are determined.

In the second technique, we observe the optical emission of the gas cloud excited by the incoming ion beam. This technique follows the one-dimensional (1D) formation and evolution of the gas cloud produced when an intense heavy-ion beam strikes the vacuum wall at normal incidence. We compare these observations with the predictions of a simple 1D model for expansion of the cloud.

II. APPARATUS

The high current experiment (HCX) [5] at Lawrence Berkeley National Laboratory is designed to explore the physics of intense heavy-ion beam transport in the context of developing a driver for heavy-ion inertial fusion energy production [6]. Typical K^+ beam current is 0.18 A in a 4 μs (flattop) beam pulse at an energy of 1 MeV (4.5×10^{12} beam ions per pulse). Pulse repetition rate is 10 seconds. The vacuum system consisted of oil-free turbo and cryopumps. The energy analyzer measurements were performed downstream of the electrostatic quadrupole injector, matching section and electrostatic transport section as described in [5]. The optical and residual gas analyzer (RGA) measurements were performed between the second and third magnetic quadrupoles of the magnetic transport section as depicted in Fig. 1, which was installed immediately downstream of the electrostatic transport section after the energy analyzer measurements were completed. The elliptical cross section of the beam pipe through the magnetic quadrupoles is 6×10 cm.

For the optical measurements, a stainless steel (type 304) target was mounted on a movable paddle and inserted

*fmbieniosek@lbl.gov

†Current address: Fermi National Accelerator Laboratory, Batavia, Illinois 60510, USA.

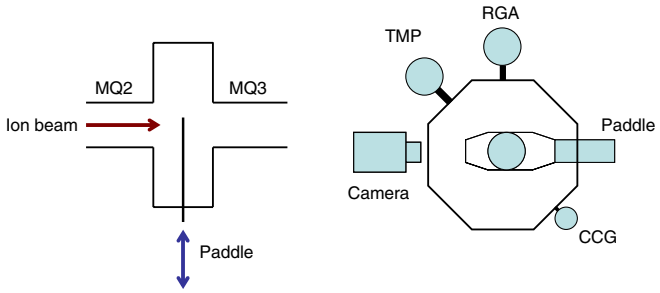

FIG. 1. (Color) Schematic of the optical and fast RGA measurement in the magnetic transport section of HCX. The ion beam enters from the left (red arrow) and passes through 4 quadrupole magnets. The paddle in the diagnostic tank between the second and third magnetic quadrupoles (MQ2 and MQ3) is inserted into the path of the beam. A cross section view of the octagonal-shaped diagnostic tank shows the relative location of the paddle and diagnostics.

into the path of the ion beam. No special cleaning techniques were used on the target. The circular target was mounted on a paddle on a sliding feedthrough that can be inserted into the path of the beam. Azimuthal locations of target and diagnostics including the high-speed CCD camera and RGA described below are indicated in Fig. 1. Pressure is monitored by the cold cathode gauge (CCG). Local pumping was provided by a turbomolecular pump (TMP) rated at 150 liter/ sec .

The optical images were taken by a high-speed image-intensified CCD camera (Princeton Instruments PI-MAX) imaging the gas cloud at a right angle to the beam. The camera is capable of taking a single gated image per beam pulse.

A Stanford research system residual gas analyzer, RGA-300, with a fast direct analog output, was installed at a port within about 40 cm of the target. It was used to measure the local gas density increase immediately after the beam pulse.

A typical time-averaged image of the beam imaged on a scintillator at the location of Fig. 1 is shown in Fig. 2. See Ref. [7] for a description of optical beam diagnostic techniques used in these measurements. Here the optical signal has been time averaged over the beam pulse for comparison with the gas cloud data.

The electrostatic energy analyzer (EEA) used in these experiments was a 90° cylindrical sector field analyzer with first-order focus [8]. The EEA has a radius of curvature of 45.72 cm, a separation between plates of 2.54 cm (Fig. 3). The deflection plate voltages to provide the 90° sector bend field for a 970-keV ion beam are ± 54 kV for K^+ and ± 27 kV for K^{++}. A drift region extends before and after the sector field to provide the first-order focus of the entrance slit at the detector plane. The entrance slit provides collimation for the measurements; its dimensions are 0.05 cm $\times$ 6.64 cm in a stainless steel foil; the slit-cup detector has an entrance slit width of 0.010 cm.

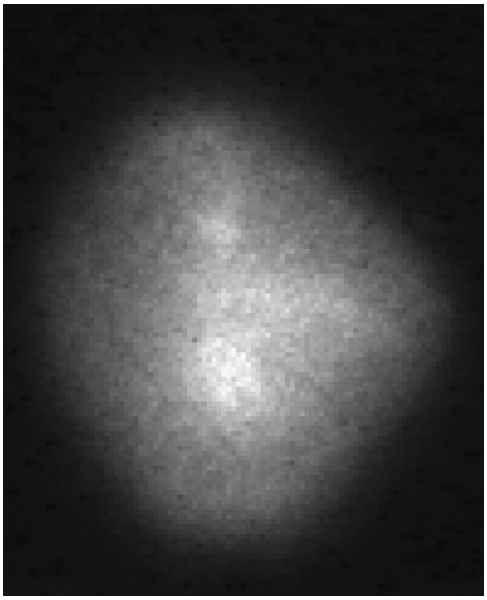

FIG. 2. Cross sectional image of the total HCX beam intensity at the location of Fig. 1. The scale for this image is 4.9 cm (horizontal) by 6.0 cm (vertical).

The EEA was mounted at the end of the diagnostic tank such that the entrance slit was 1.5 m downstream of the last HCX quadrupole. A slit-cup detector was located at the image plane of the analyzer with the 0.1-mm slit aligned on the center path between the deflecting electrodes. In addition to its utility as an energy analyzer, the EEA can distinguish a weak signal of doubly ionized K^{++} ions from the intense incident K^+ beam. This is done by operating the analyzer at exactly half of the voltage appropriate for K^+ beam ions. A 23% transparency hole plate (304 SS, 76 μm hole diameter with 152 μm separation on a hexagonal pattern) [Buckbee-Mears BE 0201 (now Internet, Inc.)] was installed on a movable drive 69 cm upstream of the analyzer entrance slit to provide higher charge-state ions for the measurement of gas production.

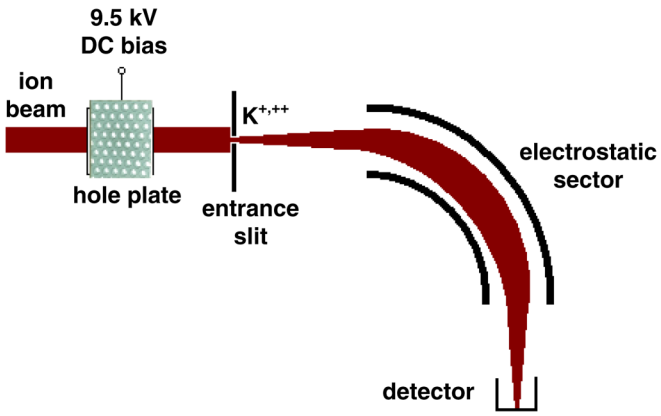

FIG. 3. (Color) Simplified schematic diagram of the electrostatic energy analyzer.

III. RESULTS

A. Composition of desorbed gas

The base pressure in the vacuum system in the absence of the beam was approximately 1×10^{-7} Torr, consisting of primarily H_2O, N_2, and O_2 gas.

RGA signals were measured for a number of atomic masses with time resolution of about 40 ms. The instantaneous time response of the signals showed a rapid increase in signal at the time of beam firing, limited by the 40-ms response of the RGA. The subsequent exponential decay rate (1/e) was 100–250 ms. A weak trend with atomic number was observed; the decay rate for small atomic numbers (1–2 amu) averaged ~130 ms; the decay rate for large atomic numbers (up to 56 amu) averaged ~230 ms.

Figure 4 shows a fast RGA spectrum for hydrogen, atomic mass unit (amu) = 2. In the mode of operation used in this scan, the RGA is centered on the given mass value, and then scans ±2 amu from that mass to yield the 40-ms oscillating behavior.

Figure 5 summarizes the zero-time intercepts of the RGA signals. These are extrapolations to time $t = 0$ from the exponential decay of the RGA signal for each ion mass. Each data point in the figure represents the zero-time intercept of the signal from a single beam pulse at the given mass number. The results indicate that the gas released is dominated by hydrogen (1 or 2 amu). The next largest peak is mass 28 (CO or N_2), and all other peaks are small. This species mix characteristic of the instantaneous wall desorption differs substantially from the baseline residual gas.

The RGA time constants may be compared with the calculated gas flow out of the diagnostic chamber, which has a volume of about $V = 14$ liters. The pumping speed S is about 100 l/s for the TMP (nominal 150 l/s connected by a short tube of about ~100 l/s), plus the conductance of the beam tubes (~ 40 l/s). This gives a time constant

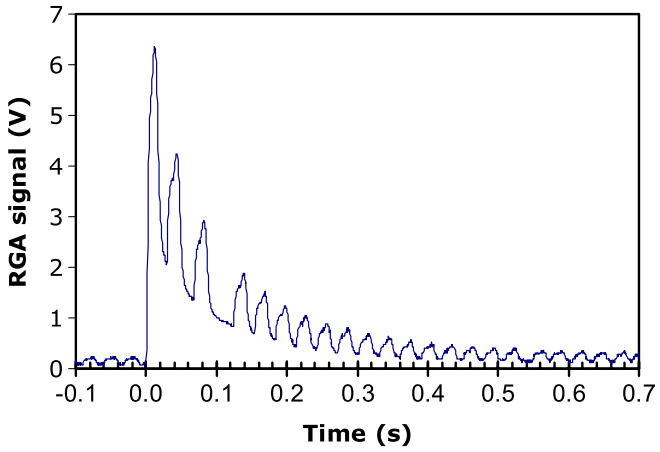

FIG. 4. (Color) Fast RGA signal from the RGA-300 for amu = 2 (hydrogen).

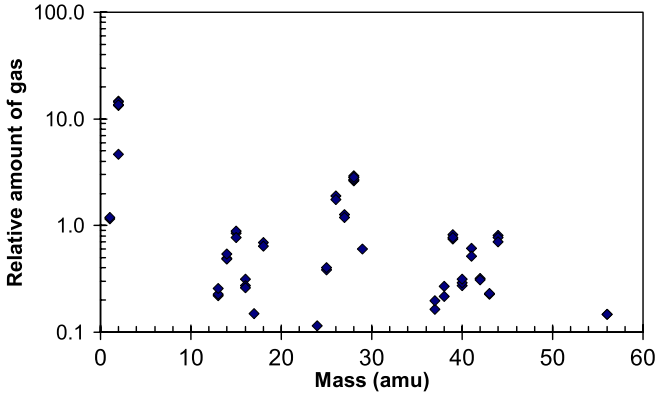

FIG. 5. (Color) Zero-time intercepts of the fast RGA signals as a function of atomic mass number amu.

$V/S \approx 100$ ms which is longer than the 40 ms time resolution of the RGA and is consistent with the measured decay rates.

At a velocity of 0.5 mm/μs, the molecules undergo on the order of 1000 collisions with the wall in 100 ms. We speculate that the difference in species mix between the ambient gas in the absence of the beam, which is dominated by H_2O, and the short-term gas cloud, which is dominated by H_2, is related to different sticking probability of the different gas species. For example, a sticking probability of 0.1% removes much of the H_2 on a 100 ms time scale.

B. Optical measurement of the gas expansion

Optical measurements of the gas cloud were performed viewing at a right angle to the beam at a plate inserted in the path of the HCX beam (Fig. 1). The beam ions interact with the gas cloud to generate light as the beam excites states in the atoms and molecules in the gas cloud. By varying the time gating of the camera, it is possible to construct a time history of the gas cloud during the beam pulse.

Emission profiles are a measure of the rate of decay of excited states of the gas molecules. During the beam pulse, the gas molecules are continuously excited by the passage of the intense ion beam. After the end of the beam pulse, some residual radiation continues to be observed with a decay time of several μs. The spectrum of this residual radiation is not the same as that of the emission during the beam pulse. The residual radiation may be due to the decay of relatively long-lived metastable excited states of the gas molecules.

A series of images taken with the PI-MAX camera at 0.5 μs intervals shows growth and decay of the gas cloud as a function of time (Fig. 6).

A line integral of the images was constructed to create what is effectively a streak camera image. These images were constructed by integrating each image vertically to generate a curve of total light intensity as a function of

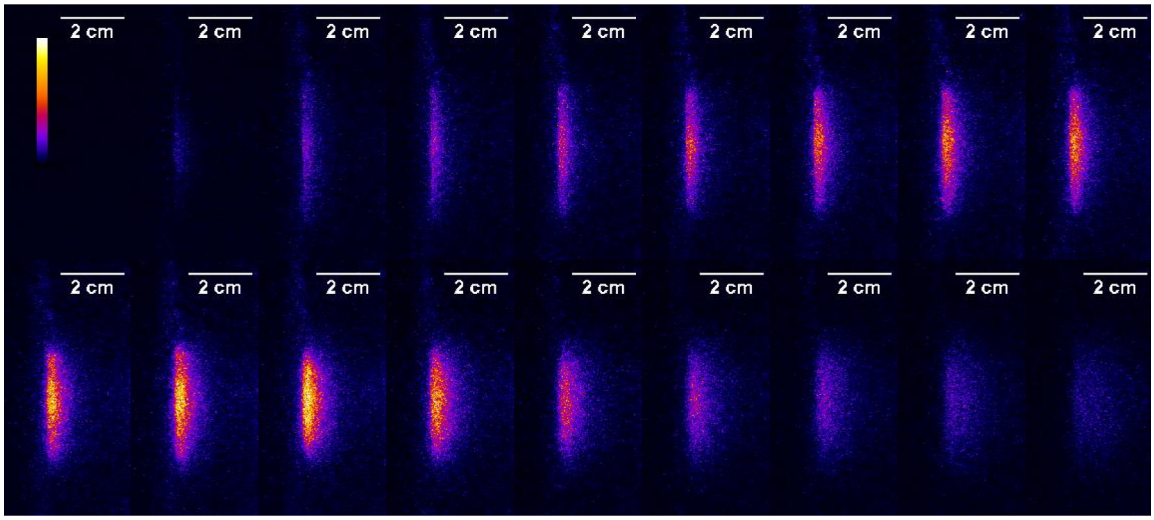

FIG. 6. (Color) Images of the gas cloud taken at 0.5 μs delay intervals.

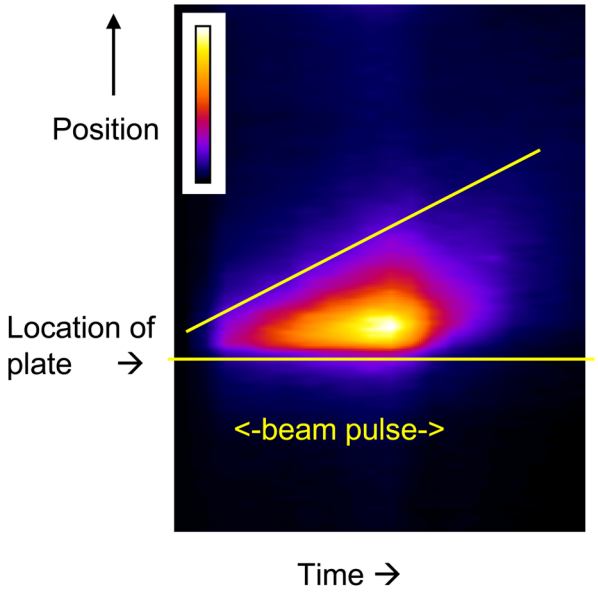

FIG. 7. (Color) Line integral of the images of Fig. 4. The sloped line indicates an expansion rate of 1.5 mm/μs. The beam pulse is 4 μs long.

horizontal distance from the target along the beam axis. Assembling the curves produces Fig. 7, which shows a false-color image of the optical signal as a function of position and time. The image shows the expansion of the cloud, with an edge expansion velocity of roughly 1.5 mm/μs. The gas cloud was imaged in three colors—blue, green, and red filters (Wratten numbers 29, 11, and 47B). The three streak images, summarized in Fig. 8, show much the same expansion velocity in the three colors, with some differences, primarily in the residual optical emission after the end of the beam pulse. The gas cloud emission was roughly uniform across the optical spectrum during the beam pulse, and it fluoresced predominantly in the green afterwards. The overall mean gas velocity was 0.5 mm/μs, consistent across the optical spectrum. This corresponds to a fixed mean directed velocity of a Maxwellian distribution $\bar{v}/4$, and is consistent with a gas cloud dominated by neutrals of a single mass or similar masses. The value for $\bar{v}/4 = \sqrt{kT/2\pi m}$ at a temperature of 20 °C is 440 m/s for molecular hydrogen H_2, and 623 m/s for atomic hydrogen H. The measured velocity corresponds to a distribution of H_2 molecules near room

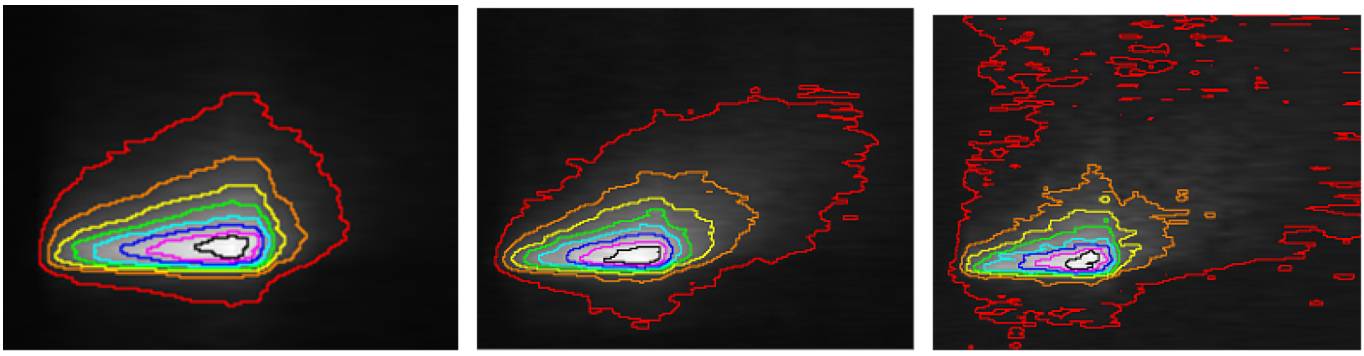

FIG. 8. (Color) Gas cloud imaged in blue, green, and red. Shown are contours of constant light intensity.

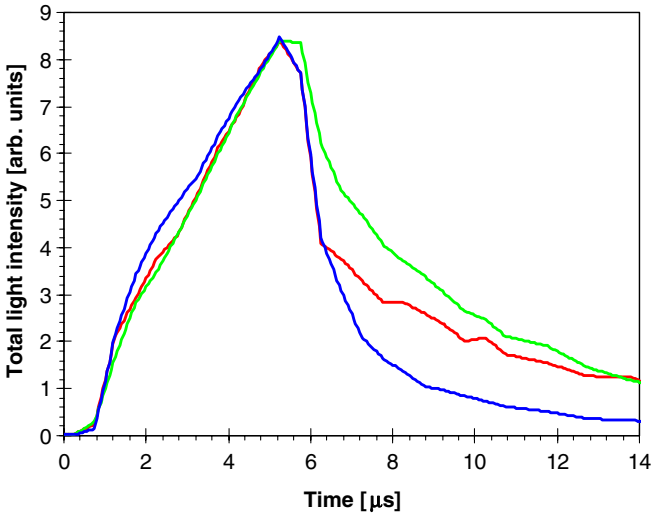

FIG. 9. (Color) Line-integrated light profiles in red, green, and blue—total emission from the entire cloud. The relative intensity of the three colors has been normalized to the peak value.

temperature; the possibility that the gas cloud is emitted in the form of predominantly atomic H is ruled out because the expansion velocity is slower than the thermal expansion velocity for an atomic hydrogen cloud. In addition, the optical emission spectrum imaged by an optical spectrometer lacked strong line structure, such as the Balmer lines of atomic hydrogen (H-alpha, H-beta, etc.). This result is consistent with the band structure of the spectrum of molecular H_2 [9].

Line-integrated total light profiles show the growth, expansion, and decay of the gas cloud [Fig. 9]; the total imaged light increased roughly linearly during the beam pulse, then decayed slowly afterwards.

C. Energy analyzer measurements

The analyzer entrance aperture was 130 cm downstream of the exit of the HCX magnetic transport section. In this field-free drift region the ion beam was allowed to expand to a beam size approximately 3 cm $\times$ 10 cm at the analyzer location, as estimated by a beam envelope code.

As the beam strikes the steel wall surrounding the holes in the hole plate or the analyzer entrance slit, gas is released from the wall. The gas forms a cloud that expands at a rate characterized by its directed velocity. For H_2, the directed velocity is 440 m/s for a gas temperature $T =$ 20 °C as discussed above. This velocity is sufficient to expand uniformly into the holes in the hole plate and into the 0.5-mm analyzer entrance slit on a time scale much less than the beam pulse length, $\tau \ll 4\ \mu$s.

Measurements discussed here were performed with the hole plate inserted in the path of the beam, upstream of the EEA. It was inserted for three reasons: (i) The hole plate can be biased to distinguish production of K^{++} at the hole plate from production at the analyzer entrance slit; (ii) the hole plate reduces the K^{++} beam intensity in the vicinity to minimize beam loading on the analyzer plates; (iii) the hole plate provides an independent K^{++} signal at greatly different source density to compare with the K^{++} signal from the analyzer entrance slit. In this way, it is possible to estimate the effect of charge exchange, as discussed below.

Measurements of the beam current transported through the analyzer were performed by adjusting the analyzer deflection voltage in 40 V increments for K^+ and 20 V increments for K^{++}, to map out the beam energy distribution as a function of time on a pulse-by-pulse basis. These increments correspond to a transverse variation of the beam at the detector location of 0.034 cm per increment.

Figure 10 shows the transported beam current taken from a scan of the K^+ beam. The raw signals from a series of measurements taken with a fixed increment in analyzer voltage were summed and scaled by the following factors to yield the total beam current transported through the analyzer, i_+:

$$i_+ = \frac{s}{wR(\delta + 1)} V,$$

where V is the detector signal in volts, w is the detector slit width (0.01 cm), R is the viewing resistor (50 Ω), s is the step increment of the measurements (0.034 cm), and δ is the secondary electron emission coefficient for the ion beam (≈ 20). The coefficient δ is determined *in situ* by providing a negative potential bias on the collector to drive secondary electron flux away from the collector and measuring the increase in signal on the collector due to the flux of secondary electrons leaving the collector.

These measurements were taken with a negatively biased collector behind the detector slit. The signal represents the sum of the ion beam current and the secondary electron current produced at the detector plate by the incident beam ions. The measured total K^+ beam signal

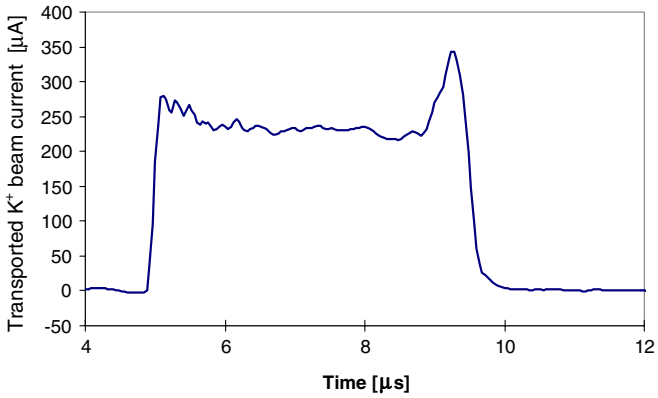

FIG. 10. (Color) Transported K^+ beam current as a function of time derived from summing the detector slit data. The total HCX beam current pulse as measured by a Faraday cup is flat; the peaks at the head and tail of the detector signal may be related to variations in beam size at the head and tail of the pulse.

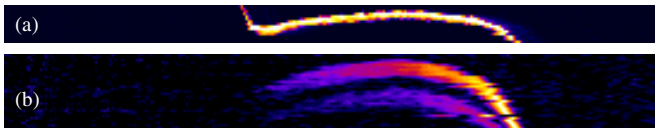

FIG. 11. (Color) (a) Intensity plot of K^+ ion signal during the beam pulse as a function of time. The vertical size of this image is 12.6 keV in beam energy. (b) Intensity plot of K^{++} ion signal during the beam pulse. The hole plate is biased to +9.4 kV. Note the two curves indicating ions from the hole plate (upper curve) and from the entrance slit (lower curve) are cut off before the end of the beam pulse because the analyzer voltage scan ends at that point. The vertical size of this image is 25.2 keV in beam energy.

corresponds to a beam current of about 230 μA transported through the analyzer.

The K^+ signal intensity as a function of time and voltage is shown in Fig. 11(a). The shape of the longitudinal beam energy distribution is described in detail in Ref. [5].

Similarly, an intensity plot of the K^{++} signal as a function of time and analyzer voltage is shown in Fig. 11(b). It is necessary to distinguish the K^{++} ions created at the entrance slit from the K^{++} ions created at the hole plate. They can be distinguished by the different energy of the two populations. The plot clearly shows two distributions; the upper distribution corresponds to the K^{++} ions created at the hole plate, with a bias of 9.5 kV, and the lower distribution corresponds to the K^{++} ions created at the entrance slit, which is grounded.

Figure 12 shows the signal taken from a scan of the K^{++} signal, again taking into account the known step size increments. It has been scaled in a manner similar to that described above for the K^+ signal:

$$i_{++} = \frac{s}{wR(\delta + 2)} \frac{1}{A_g} V.$$

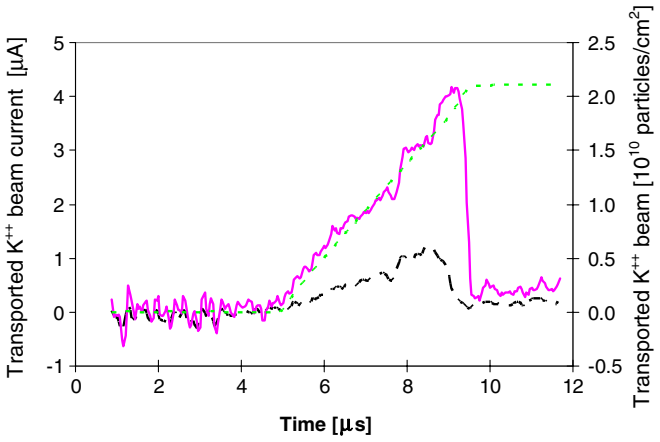

FIG. 12. (Color) This is the total K^{++} ion current (solid magenta), K^{++} current from the entrance slit only (long dashed black), and the integrated number of transported K^+ ions in the analyzer (short dashed green).

These measurements were also taken with a negatively biased collector, and with an additional amplifier of gain $A_g = 50$. The total K^{++} particle current at the peak is 3.5 μA. After the upper distribution from the hole plate is removed, the peak particle current from the slit is 1.14 μA.

The ratio of the two ion currents (K^{++} from the analyzer entrance slit)/(K^+ from the beam) is 0.005. This ratio is a direct measure of the product of the line density of the gas cloud at the entrance slit, and the ionization cross section, $\langle nl \rangle \sigma_{12}$. The time-integrated flux density of incident beam ions at the time of the peak K^{++} signal (the K^{++} signal was truncated in taking the data at late times) is $n_b = \frac{1}{A_{\text{slit}} e} \int i_+ dt = 1.6 \times 10^{10}$ cm^{-2} where $A_{\text{slit}} = 0.332$ cm^2 is the area of the slit. Note that the integral is taken up to the time of the peak of the K^{++} signal, not the end of the K^+ pulse.

Note from the RGA data that the gas cloud is dominated by H_2. The ionization cross section σ_{12} for a K^+ beam ($K^+ \rightarrow K^{++}$) on H_2 has been measured up to 600 keV; σ_{12} at 600 keV is $\sigma = 1.14 \times 10^{-16}$ cm^2 [10]. Since the ionization cross section dependence on energy is relatively flat in this range, we use this value for σ_{12} at the experimental beam energy (970 keV).

For $\langle nl \rangle \sigma_{12} = 0.005$, and $\sigma_{12} = 1.14 \times 10^{-16}$ cm^2, the line density of gas is $\langle nl \rangle = 4.4 \times 10^{13}$ cm^{-2}. The number of gas particles at the slit per incident ion beam is then simply the ratio $\langle nl \rangle / n_b = 2740$. The rate of K^{++} production is directly proportional to the instantaneous gas line density and the beam current; both increase linearly during the beam pulse, as seen in Fig. 12. At the end of the beam pulse the K^{++} current also drops to zero as expected.

IV. SOURCES OF ERROR IN THE MEASUREMENT

A. Depletion due to charge exchange

Charge exchange ($K^{++} \rightarrow K^+$) is an exchange of a single electron between the doubly charged K^{++} ion and a neutral gas molecule. Neglecting other possible charge-changing reactions, it involves a two-step process in which an incident K^+ ion is first ionized to K^{++} in the gas cloud; then the K^{++} ion recaptures an electron from a gas molecule before leaving the gas cloud. If the rates for both reactions are small $\langle nl \rangle \sigma \ll 1$, then the K^{++} is created uniformly throughout the gas cloud, and the average path length traversed by a K^{++} ion is $\langle nl \rangle / 2$. The fraction of the K^{++} ions that undergoes charge exchange is then $\frac{1}{2} \langle nl \rangle \sigma_{21}$.

The charge exchange process is energetically favorable and the cross sections tend to be large. The closest available data for the measured charge-changing cross section is $\sigma_{21} = 8 \times 10^{-16}$ cm^2 for K^{++} on N_2 and 3×10^{-15} cm^2 at 120 keV for K^{++} on O_2 [11]. In addition, Betz [12] shows that the equilibrium charge fraction for a 1-MeV potassium beam in gas is approximately 1, also indicating that σ_{21} is large. Using the larger of the two data points

from Ref. [11], charge exchange would deplete only 2% of the K^{++} ions created at the analyzer entrance slit.

In contrast, the intensity of K^{++} ions created at the hole plate is depleted from the amount expected based simply on the beam current density. The beam envelope model indicates that the incident beam intensity and thus line density of liberated gas at that location should be about 20 times larger than at the analyzer entrance slit. The higher gas density should lead in turn to both a higher K^{++} ion flux, and a higher charge exchange fraction, estimated in the range of 40%. In the absence of charge exchange, and taking into account the transparency of the hole plate, the signal from the hole plate should be about $20 \times 0.23 = 4.6$ times larger than the signal from the slit. In fact, the signal from the hole plate is about a factor of 4 larger early in the pulse, and a factor of 2 larger late in the pulse. The amount of observed depletion of K^{++} created at the hole plate is consistent with the expectation that the charge-changing cross section at 970 keV is comparable to that at the measured data point (120 keV). Because of the large depletion, analysis of K^{++} created at the hole plate would underestimate gas production. Thus, the population of K^{++} from the hole plate is not used in the determination of gas production.

B. Penetration of gas through and behind the slit

The presence of the slit reduces the transient local density of the gas cloud. The density perturbation may be estimated by considering the horizontal position x of a Gaussian distribution of particles generated at each point x_i along the surface of the wall at time t after the particle distribution is generated:

$$g(x, x_i) = \exp\left[-\frac{m}{2kT}\left(\frac{x - x_i}{t}\right)^2 \right],$$

where $(x - x_i)/t = v_x(t)$ represents the x-directed velocity of the molecule. The local gas density in the vicinity of the slit at time t is the integral

$$f(x) = \int_{-\infty}^{a} g(x, x_i)dx_i + \int_{b}^{\infty} g(x, x_i)dx_i,$$

where a and b represent the locations of the edges of the slit. The gas density averaged over the slit $\bar{h}_{\text{slit}}$ at time t is

$$\bar{h}_{\text{slit}} = \frac{1}{b - a}\int_{a}^{b} f(x)dx.$$

Finally, if gas production is a function of time, $h = h(t)$, the slit-averaged density is the convolution

$$\bar{n}_{\text{slit}}(t) = \int_{0}^{t} \bar{h}_{\text{slit}}(t - \tau)n(\tau)d\tau.$$

For a constant beam current-density pulse, $j = \text{const}$ for $0 < t < t_{\text{pulse}}$, the gas density follows the integral of the current pulse: $n(t) = n_0 t/t_{\text{pulse}}$, for $t < t_{\text{pulse}}$ and $n(t) = n_0$, for $t \geq t_{\text{pulse}}$. The ratio of the calculated slit-averaged density $\bar{n}_{\text{slit}}(t)$ to the gas density at the edge of the slit during the beam pulse for H_2 gas at 20 °C is ~0.9. Thus, a small correction of 1/0.9 due to this effect should be applied to the estimate for gas production. The gas desorption coefficient is therefore approximately 3000 gas molecules per beam ion.

V. MODEL OF GAS PROFILE

The intensity of the incident beam pulse is 5.1×10^{12} ions per pulse. If the desorption coefficient is independent of beam intensity, the number of gas molecules released at the target is 1.53×10^{16} per beam pulse. A comparison between the optical signal from the gas cloud and a line integral through the beam cross section of Fig. 2 shows similarity (Fig. 13), indicating that the assumption of linearity is reasonable. The peak beam intensity based on the image of Fig. 2 is 7×10^{11} cm^{-2}, indicating a peak gas cloud intensity of 2×10^{15} cm^{-2}. Taking 1×10^{15} cm^{-2} for a monolayer, the amount of gas released per pulse at the center of the beam is about 2 monolayers. The density of gas near the surface at an average rate of expansion 0.5 mm/μs peaks at about 1×10^{16} cm^{-3}. At this density the mean-free path for H_2 molecules near the surface is <1 mm.

We model the expansion of the gas cloud from the wall as a 1D expansion, i.e., the distance from the wall is less than the transverse extent of the beam at the target. Models for 1D expansion of a desorbed gas into a vacuum are described in detail in [13,14]. In the case of a sufficiently intense release of gas, i.e., when the mean-free path is

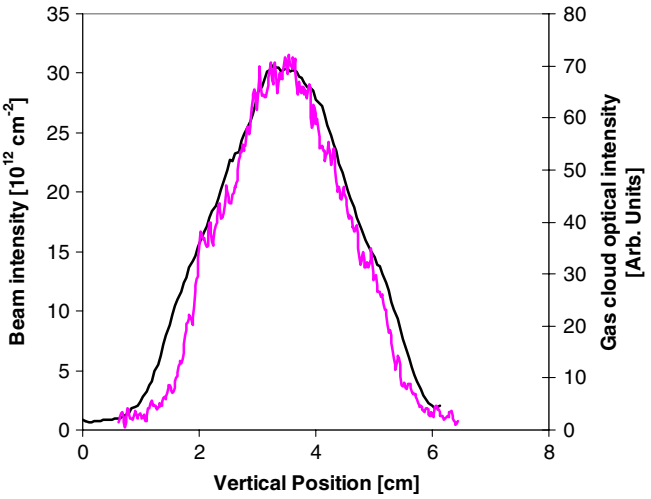

FIG. 13. (Color) Comparison between beam intensity integrated along the horizontal direction (black) of the beam of Fig. 2, and the optical emission from the gas cloud integrated along the horizontal direction (magenta) of the gas cloud at the end of the beam pulse (Fig. 6), both plotted with respect to vertical position.

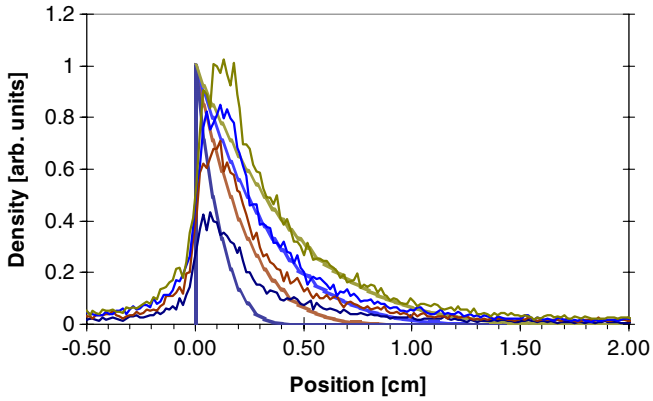

FIG. 14. (Color) Experimental profile of light intensity of gas cloud at 1 μs intervals during the beam pulse; density profile from 1D gas cloud model for H_2 gas at 20 °C. The smooth shaded curves represent the model profiles.

smaller than the macroscopic scale length, the gas dynamic equations take on a particularly simple form. Assume that the gas obeys the adiabatic law $n = \text{const} \cdot c^{2/(\gamma-1)}$, where γ is the ratio of specific heats, n is the density, and c is the velocity of sound. For time $t < t_{\text{pulse}}$, the gas flow is controlled by the velocity at the Knudsen layer on the surface of the target, $u_k = \sqrt{\gamma(kT_k/m)}$. The constant T_k is the temperature of the surface layer. Referring to Eq. (12) of Ref. [14], the density profile can be written as

$$n(x, t) = n_0\left(1 - \frac{\gamma - 1}{\gamma + 1}\frac{x}{t}\right)^{2/(\gamma-1)}.$$

Note that contours of constant density are straight lines on an x vs t plot, in agreement with the measured contours of Fig. 8. The model density profiles are plotted for H_2 gas ($\gamma = 1.4$), together with the experimental image intensity profiles, in Fig. 14. Measured gas expansion is generally slower than predicted by the model for 20 °C; comparison between the data and the model suggests a Knudsen temperature much lower than the surface temperature.

After the end of the beam pulse, $t > t_{\text{pulse}}$, the behavior becomes more complicated and depends on the reflection properties of the gas particles on the wall surface. Reflection of the particles leads to a wave that travels into the gas cloud beginning at $t = t_{\text{pulse}}$ at the surface.

In the low-density case of a beam halo scraping the walls, the evolution of gas will be similar in form and may be modeled by the rate of expansion of the gas molecules into the vacuum.

VI. DISCUSSION

The rate of gas production is measured with excellent time resolution. The results verify that, as expected, large amounts of gas are released from the wall in the beam-wall interaction. The gas production is shown to be instantaneous and directly proportional to the incident ion beam intensity up to the intensity used in these experiments. These techniques are not sensitive to gas desorption after the beam pulse.

Measurements at other laboratories such as BNL, CERN, GSI, etc. show desorption yields ranging over many orders of magnitude [3,4,15–19]. The yield of desorbed gas molecules is expected to vary widely with parameters such as beam energy, type, and charge state of the beam ions, impact angle, and wall surface conditions including cleanliness, surface roughness, history, baking, and type of material. Therefore the measured absolute gas yield should be considered an approximate guide to the yield under any given set of conditions.

The yield derived here, ~3000 desorbed gas molecules per beam ion at normal incidence, may be compared with other measurements of gas production [3,4,15–19]. Published measurements vary widely over a wide range. There are several possible reasons for the wide range and discrepancy, in addition to the effects of surface condition. One reason is that many measurements are typically taken at near grazing incidence, where the numbers are expected to be larger than at normal incidence. For example, the gas desorption coefficient of 10 000 for similar beam conditions (unbaked target) at grazing incidence presented in Ref. [3] extrapolates to about 3000 at normal incidence. Another reason is that time-integrated gas production monitored by a vacuum pressure gauge typically measures gas after one or several bounces off the vacuum wall, whereas the technique described here measures the instantaneous local gas production during the beam pulse.

This technique has application as an alternative to the conventional techniques for measuring heavy-ion-beam-induced adsorption of gas from the wall. The advantage is that the measurement is direct and instantaneous during the time of the beam pulse. Further measurements that can be made include: (i) instantaneous gas production as a function of angle of incidence and angle of emission by passing the beam through a pivoted slit or aperture plate, (ii) effects of wall material and condition on gas cloud species and quantity, (iii) desorption from a NEG coating or cryogenic target, and (iv) absolute calibration of the RGA for direct comparison of partial pressure measurements with the instantaneous gas desorption measurements described here.

ACKNOWLEDGMENTS

The authors gratefully acknowledge the support of W. Greenway, T. Katayanagi, and the LBNL technical staff. This work was performed under the auspices of the U.S. Department of Energy by University of California, Lawrence Livermore, and Lawrence Berkeley National Laboratories under Contracts No. W-7405-Eng-48 and DE-AC03-76SF00098.

[1] A. W. Molvik, H. Kollmus, E. Mahner, M. Kireeff Covo, M. C. Bellachioma, M. Bender, F. M. Bieniosek, E. Hedlund, A. Krämer, J. Kwan, O. B. Malyshev, L. Prost, P. A. Seidl, G. Westenskow, and L. Westerberg, Phys. Rev. Lett. **98**, 064801 (2007), and references therein.

[2] Proceedings of the Workshop on Electron-Cloud Simulations for Proton and Positron Beams (ECLOUD04), Napa, California, 2004, edited by M. Furman, http://mafurman.lbl.gov/ECLOUD04_proceedings.

[3] A. W. Molvik, M. Kireeff Covo, F. M. Bieniosek, L. R. Prost, P. A. Seidl, D. Baca, A. Coorey, and A. Sakumi, Phys. Rev. ST Accel. Beams **7**, 093202 (2004).

[4] S. Y. Zhang, "ICFA Workshop on Beam Induced Pressure Rise in Rings," http://www.c-ad.bnl.gov/icfa, 2003.

[5] L. R. Prost, P. A. Seidl, F. M. Bieniosek, C. M. Celata, A. Faltens, D. Baca, E. Henestroza, J. W. Kwan, M. Leitner, W. L. Waldron, R. Cohen, A. Friedman, D. Grote, S. M. Lund, A. W. Molvik, and E. Morse, Phys. Rev. ST Accel. Beams **8**, 020101 (2005).

[6] B. G. Logan, F. M. Bieniosek, C. M. Celata, E. Henestroza, J. W. Kwan, E. P. Lee, M. Leitner, P. K. Roy, P. A. Seidl, S. Eylon, J.-L. Vay, W. L. Waldron, S. S. Yu, J. J. Barnard, D. A. Callahan, R. H. Cohen, A. Friedman, D. P. Grote, M. Kireeff Covo, W. R. Meier, A. W. Molvik, S. M. Lund, R. C. Davidson, P. C. Efthimion, E. P. Gilson, L. R. Grisham, I. D. Kaganovich, H. Qin, E. A. Startsev, D. V. Rose, D. R. Welch, C. L. Olson, R. A. Kishek, P. O'Shea, I. Haber, and L. R. Prost, Nucl. Fusion **45**, 131 (2005).

[7] F. M. Bieniosek, S. Eylon, A. Faltens, A. Friedman, J. W. Kwan, M. A. Leitner, A. W. Molvik, L. Prost, P. K. Roy, P. A. Seidl, and G. Westenskow, Nucl. Instrum. Methods Phys. Res., Sect. A **544**, 268 (2005).

[8] R. E. Warren, J. L. Powell, R. G. Herb, Rev. Sci. Instrum. **18**, 559 (1947).

[9] H. G. Gale, G. S. Monk, and K. O. Lee, Astrophys. J. **67**, 89 (1928).

[10] I. Alvarez, C. Cisneros, C. F. Barnett, and J. A. Ray, Phys. Rev. A **13**, 1728 (1976).

[11] H. H. Lo and W. L. Fite, Atomic Data **1**, 305 (1970).

[12] H. D. Betz, IEEE Trans. Nucl. Sci. **NS-18**, 1110 (1971)

[13] D. Sibold and H. M. Urbassek, Phys. Rev. A **43**, 6722 (1991).

[14] D. Sibold and H. M. Urbassek, Phys. Fluids A **4**, 165 (1992).

[15] E. Mahner *et al.*, Phys. Rev. ST Accel. Beams **6**, 013201 (2003).

[16] H. Kollmus, M. C. Bellachioma, M. Bender, A. Krämer, J. Kurdal, and H. Reich-Sprenger, Vacuum Issues of SIS18 Upgrade at GSI, Proc. 2006 European Particle Accelerator Conference, Paper TUPCH174, available at the JACOW web site: http://accelconf.web.cern.ch/accelconf/.

[17] E. Mahner, J. Hansen, D. Kuechler, M. Malabaila, and M. Taborelli, Phys. Rev. ST Accel. Beams **8**, 053201 (2005).

[18] R. Behrisch, V. M. Prozesky, H. Huber, and W. Assman, Nucl. Instrum. Methods Phys. Res., Sect. B **118**, 262 (1996).

[19] H. A. Davis, R. T. Olson, and D. C. Moir, Phys. Plasmas **10**, 3351 (2003).